ARTICLE

Check for updates

Machine learning autonomous identification of magnetic alloys beyond the Slater-Pauling limit

Yuma Iwasaki [1,2,3✉], Ryohto Sawada[1], Eiji Saitoh[4,5,6,7,8] & Masahiko Ishida[1,3]

Discovery of new magnets with high magnetization has always been important in human history because it has given birth to powerful motors and memory devices. Currently, the binary alloy Fe_3Co_1 exhibits the largest magnetization of any stable alloys explained by the Slater-Pauling rule. A multi-element system is expected to include alloys with magnetization beyond that of Fe_3Co_1, but it has been difficult to identify appropriate elements and compositions because of combinatorial explosion. In this work, we identified an alloy with magnetization beyond that of Fe_3Co_1 by using an autonomous materials search system combining machine learning and ab-initio calculation. After an autonomous and automated exploration in the large material space of multi-element alloys for six weeks, the system unexpectedly indicated that Ir and Pt impurities would enhance the magnetization of FeCo alloys, despite both impurity elements having small magnetic moments. To confirm this experimentally, we synthesized $Fe_xCo_yIr_{1-x-y}$ and $Fe_xCo_yPt_{1-x-y}$ alloys and found that some of them have magnetization beyond that of Fe_3Co_1.

[1] System Platform Research Laboratories, NEC Corporation, Kawasaki 211-8666, Japan. [2] PRESTO, JST, Saitama 322-0012, Japan. [3] NEC-AIST Quantum Technology Cooperative Research Laboratory, National Institute of Advanced Industrial Science and Technology (AIST), Tsukuba 305-8568, Japan. [4] Institute for Materials Research, Tohoku University, Sendai 908-8577, Japan. [5] Center for Spintronics Research Network, Tohoku University, Sendai 980-8577, Japan. [6] Department of Applied Physics, University of Tokyo, Tokyo 113-8656, Japan. [7] Advanced Institute for Materials Research, Tohoku University, Sendai 908-8577, Japan. [8] Advanced Science Research Center, Japan Atomic Energy Agency, Tokai 319-1195, Japan. ✉email: y.iwasaki0827@gmail.com

Materials with a high magnetization are indispensable for information storages, motors, sensors, actuators, and other electric devices[1,2]. The metastable iron nitride α″-Fe$_{16}$N$_2$ is believed to have the highest magnetization[3]. However, it decomposes at a relatively low temperature (~250 °C), and this thermal instability precludes practical application of the material[4]. Some of metastable alloys, where the crystal structure and lattice constant are fixed by force, also exhibit the high magnetization. For instance, ultrathin epitaxial films of Fe$_x$Co$_y$Mn$_z$ have very high magnetization, but it was not achieved in stable states such as a non-epitaxial film and bulk[5]. Therefore, a stable alloy with a high magnetization has been desired for practical applications. As shown by the Slater–Pauling curve (Supplementary Fig. S1), the binary alloy Fe$_3$Co$_1$ has the highest magnetization of any stable alloy, called the Slater–Pauling limit[6]. Generations of scientists have tried to discover a stable magnetic alloy beyond the Fe$_3$Co$_1$ limit by investigating multi-element alloys, but it is difficult to study multi-element alloys comprehensively because combinatorial explosion requires us to carry out a quite large number of simulations and/or experiments.

Multi-element materials are often investigated by machine learning, which is used because of its ability for multidimensional analysis[7–17]. It is noteworthy that machine learning has already been used to develop materials for magnets[18,19], batteries[20,21], superconductors[22,23], ferroelectrics[24,25], thermoelectrics[26,27], and photovoltaics[28,29]. Data-driven machine learning approaches should shed new light on our knowledge of materials and thus bring about the discovery of unexpected novel materials.

Sumita et al.[30] and Sawada et al.[31] have recently suggested an autonomous materials search system that simulates the entire process of conventional manual materials search shown in Fig. 1a: (I) fabricate materials, (II) evaluate their properties, and (III) decide on next target materials. Figure 1b shows the autonomous materials search system combining machine learning and ab-initio simulation technologies. The virtual materials fabrication step (I′) and virtual materials evaluation step (II′) are simulated using the ab-initio method, which predicts various material properties from the composition and crystal structure information. For the step deciding the next target composition/structure (III′), machine learning techniques such as Bayesian optimization[30] and game tree search[31] are used. Machine learning is used to statistically decide the next target material from the data obtained in step II′, with consideration of the trade-off between exploration and exploitation by using an upper confidential bound strategy (UCB)[31]. In other words, these machine learning techniques are adjusted to select a next target material with a better property from materials dissimilar to those that have already been tried in steps I′ and II′. Since the amount of learning data increases with repetition of this automated cycle, the machine learning model gradually improves and suggests better materials.

In this work, the autonomous materials search system indicated that Ir and Pt impurities would enhance the magnetization of FeCo alloys after the autonomous and automated exploration in the large material space of multi-element alloys. The performance of these alloys was confirmed by both experiments and theories.

Results

Machine learning-based autonomous materials search. In the work presented here we used the autonomous materials search system to identify a multi-element alloy with high magnetization. To find a potential high-magnetization alloy, the autonomous system was set to the task of optimizing the composition of a disordered multi-element alloy (Fe$_a$Co$_b$Ni$_c$Ru$_d$Rh$_e$Pd$_f$Ir$_g$Pt$_h$) with a body-centered cubic (bcc) crystal structure. The settings, including the selection of elements and structure, were determined by a simple pre-simulation (see Methods section and Supplementary Fig. S2). For the ab-initio simulation parts (I′ and II′), we used the Korringa–Kohn–Rostoker coherent potential approximation (KKR-CPA) method because it is difficult to simulate multi-element alloys by using common DFT methods such as the projector-augmented wave (PAW) method. For example, when using the common DFT methods, to simulate the binary alloy Fe$_{51}$Co$_{49}$ we have to make a very large unit cell, calculation of which is not feasible. The KKR-CPA, where the CPA deals with random (disordered) material systems and allows us to simulate band structures of multi-element materials with a single unit cell, is known for its good agreement with experimental results, especially in multi-element alloy systems[32–35]. The magnetic moment, which is roughly proportional to magnetization, was calculated
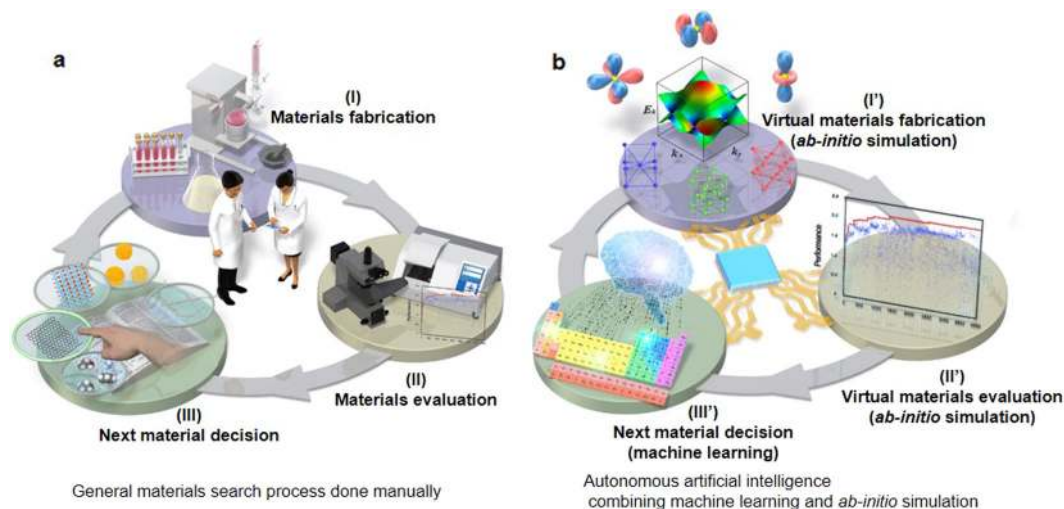

Fig. 1 Concept of autonomous materials search system. a Conventional materials search process done manually following a cycle comprising (I) a materials fabrication step, (II) a materials evaluation step, and (III) a decision step for selecting the next target material. **b** Autonomous materials search system in which the conventional process of materials search is simulated using computation technologies including ab-initio simulation and machine learning. The virtual materials fabrication step (I′) and virtual materials evaluation step (II′) are simulated using ab-initio simulation. The decision step for the next target material (II′) is simulated using machine learning such as the game tree algorithm. This autonomous system automatically grows smarter as the amount of data acquired during the automated development cycle increases and eventually it finds a better material.
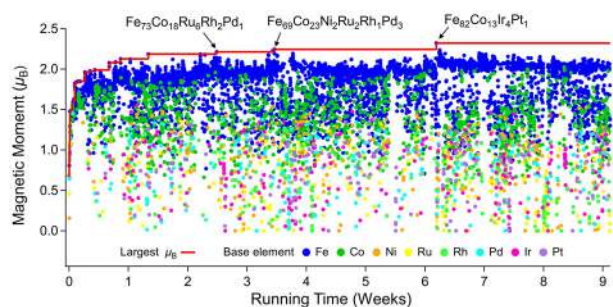
Fig. 2 Growth of autonomous materials search system. Growth of the autonomous materials search system for an alloy with a large magnetic moment. Magnetic moment data were plotted for each search cycle shown in Fig. 1b. Colors of data points show the base element of the alloys. After some time, the autonomous system was able to find a better composition for a disordered multi-element alloy ($Fe_aCo_bNi_cRu_dRh_ePd_fIr_gPt_h$) with a large magnetic moment due to an increase in the amount of data for learning. After 6 weeks (strictly, 43 days) of growth, the autonomous system arrived at $Fe_{82}Co_{13}Ir_4Pt_1$, not the composition of the alloy at the top of the Slater–Pauling curve ($Fe_{75}Co_{25}$).

using the KKR-CPA and the calculated composition values (a, b, c, d, e, f, g, and h) decided by the machine learning part (III′) using the game tree algorithm[31]. Details of the algorithms and their parameters can be found in the Methods section.

We ran the autonomous system for 9 weeks. The growth progress is illustrated in Fig. 2, where the magnetic moment data are plotted per cycle shown in Fig. 1b. Over time, as the available learning data increased, the system was able to suggest compositions for alloys with larger magnetic moments. It is particularly noteworthy that the autonomous system sometimes tested material compositions with small magnetic moments, clearly demonstrating that it considered both exploration and exploitation during the multidimensional virtual search. Some low-score data were necessary for the global optimization process because diversity (dispersion) of the learning data is essential for constructing a good machine learning (game tree) model.

The red line in Fig. 2 shows the maximum magnetic moment at each point in time. Eventually, after 6 weeks of growth, an alloy with the largest magnetic moment was suggested: $Fe_{82}Co_{13}Ir_4Pt_1$. It is only reasonable that Fe and Co are its main components because $Fe_{75}Co_{25}$ is the known alloy with the largest magnetic moment. However, the presence of Ir and Pt impurities in the material is seemingly inconsistent with chemical intuition because both elements have small magnetic moments, which would be expected to reduce the magnetic moment of the alloy. In other words, the autonomous materials search system suggested an unexpected alloy with high magnetization.

Experimental confirmation by combinatorial methods. To confirm the effect of Ir and Pt impurities experimentally, we synthesized $Fe_xCo_yIr_{100-x-y}$ and $Fe_xCo_yPt_{100-x-y}$ ternary alloys and evaluated their magnetization. For comparison, the ternary alloy $Fe_xCo_yNi_{100-x-y}$ was also investigated because Ni is the element with the third largest magnetic moment (after Fe and Co). To investigate the composition dependency within the ternary alloys, we have carried out combinatorial experiments[36,37] using composition-spread thin films on SiO_2/Si, each mapping a large fraction of the alloy's composition range on one library wafer. Figure 3a shows the conceptual image of combinatorial sputtering, where the use of three sputter guns and an automated moving mask enables synthesis of a linear composition-spread thin film[36–38]. Figure 3b shows the composition map of an

$Fe_xCo_yIr_{100-x-y}$ composition-spread thin film. For the many sampling points shown as black spots in Fig. 3b, we carried out combinatorial X-ray diffraction (combi-XRD) experiments and longitudinal magneto-optic Kerr effect (combi-MOKE)[39] experiments. Figure 3c shows the results of combi-XRD experiments with $Fe_xCo_yIr_{100-x-y}$ composition-spread samples. As an example, Fig. 3d shows the XRD pattern of $Fe_{68.1}Co_{26.2}Ir_{5.7}$ (bottom right point in Fig. 3b). All of the $Fe_xCo_yIr_{100-x-y}$, $Fe_xCo_yPt_{100-x-y}$, and $Fe_xCo_yNi_{100-x-y}$ XRD curves are shown in Supplementary Fig. S3. It is noteworthy that an Fe-bcc(200) peak is much larger than an Fe-(110) peak. This is due to the annealing process, which increases the mobility of atoms. Then the equilibrium state of an island is easy to attain, and the island prefers (200) orientation[40]. Figure 3e shows the results of combi-MOKE experiments with $Fe_xCo_yIr_{100-x-y}$ composition-spread samples. As an example, Fig. 3f shows the MOKE curves of $Fe_{68.1}Co_{26.2}Ir_{5.7}$ (bottom right point in Fig. 3b). Note that the vertical axis value in Fig. 3f is normalized by the maximum MOKE intensity of pure Fe (top left point in Fig. 3b). The amplitude of a MOKE curve is proportional to saturation magnetization M_s[41]:

$$M_s \propto M_{MOKE} = \frac{I_{max}^{MOKE} - I_{min}^{MOKE}}{2},$$

where M_{MOKE} is the amplitude of the MOKE curve and I_{max}^{MOKE} and I_{min}^{MOKE} are respectively the maximum and minimum values of the normalized MOKE intensity. As with the $Fe_xCo_yIr_{100-x-y}$ composition-spread thin film, we also performed the combi-MOKE experiment with the $Fe_xCo_yPt_{100-x-y}$ and $Fe_xCo_yNi_{100-x-y}$ samples. Figure 3g–i show the composition gradients of $Fe_xCo_yIr_{100-x-y}$, $Fe_xCo_yPt_{100-x-y}$, and $Fe_xCo_yNi_{100-x-y}$ composition-spread thin films. All of the MOKE curves are shown in Supplementary Fig. S4.

Figure 3j–l show M_{MOKE} color maps of $Fe_xCo_yIr_{100-x-y}$, $Fe_xCo_yPt_{100-x-ym}$, and $Fe_xCo_yNi_{100-x-y}$, respectively. It was found that small amounts of Ir and Pt impurities enhance the M_{MOKE}, while Ni impurity monotonically decreases the M_{MOKE}. To clarify this, Fig. 3m shows M_{MOKE} of $(Fe_{75.2}Co_{24.8})_{1-x}Ir_x$, $(Fe_{75.3}Co_{24.7})_{1-x}Pt_x$, and $(Fe_{71.1}Co_{28.9})_{1-x}Ni_x$ along dotted arrows in Fig. 3j–l, respectively. The dark-blue solid line and blue dotted line in Fig. 3m show theoretical M_{MOKE} values of pure Fe ($M_{MOKE}^{Fe} = \frac{m_{Fe}}{m_{Fe}} = 1$) and $Fe_{75}Co_{25}$ ($M_{MOKE}^{FeCo} = \frac{m_{Fe75Co25}}{m_{Fe}} \approx 1.136$), where m_{Fe} and $m_{Fe75Co25}$ are magnetic moments of Fe and $Fe_{75}Co_{25}$, respectively. It is clearly seen that the $(Fe_{75.2}Co_{24.8})_{1-x}Ir_x$ exhibit large M_{MOKE} beyond M_{MOKE}^{FeCo}.

Similar results were also obtained by another experiment, a superconducting quantum interference device (SQUID)[42] experiment. Figure 3n shows magnetization curves of $Fe_{73.2}Co_{24.2}Ir_{2.6}$ (whose M_{MOKE} is the largest in Fig. 3j), $Fe_{84.0}Co_{12.0}Pt_{4.0}$ (whose M_{MOKE} is the largest in Fig. 3k), $Fe_{75.2}Co_{24.8}$, and pure Fe at room temperature ($T = 300$ K). As with the case of the MOKE experiments, the magnetic field is applied along an in-plane direction. It is clearly seen that inserting Ir and Pt impurity into FeCo alloy enhances magnetization. Figure 3o shows the results of SQUID experiments at a low temperature (5 K). As at room temperature, we can see clear enhancement of magnetization by Ir and Pt impurities. These magnetization values obtained in the SQUID experiments still have rooms for improvement by fabrication process optimization, such as optimization of annealing temperature and time.

These experimental confirmations were constrained to ternary systems because it was difficult to fabricate quaternary alloys by using our combinatorial sputter system. In the future the quaternary alloy $Fe_{82}Co_{13}Ir_4Pt_1$ predicted by the autonomous materials search should be fabricated and investigated for a synergistic effect of Ir and Pt impurities experimentally.
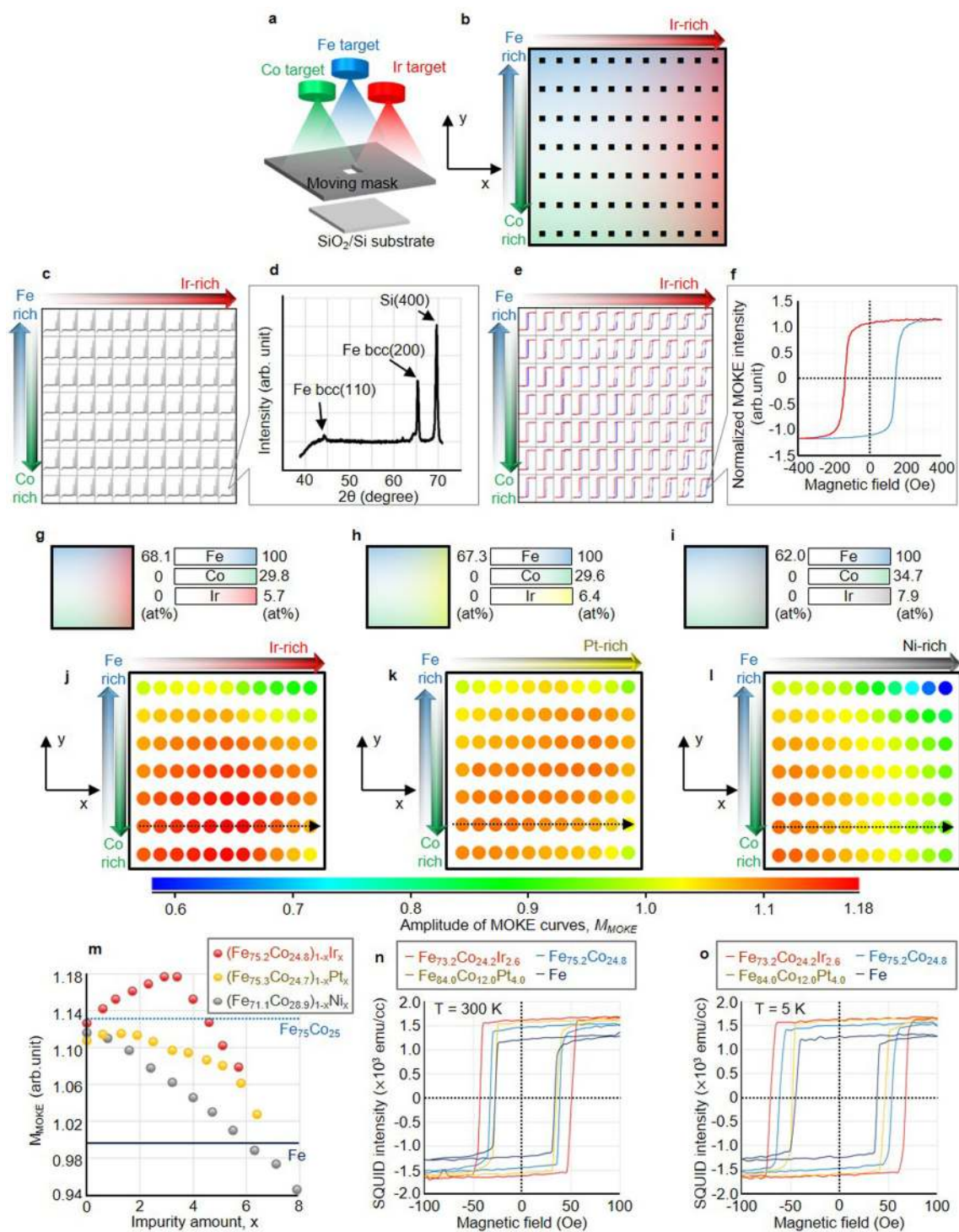
Theoretical confirmation by ab-initio simulation. In addition to the two experimental confirmations, theoretical confirmation by ab-initio simulation (KKR-CPA) was also conducted. Figure 4a, b, c show ternary plots of magnetic moment of $Fe_xCo_yIr_{100-x-y}$, $Fe_xCo_yPt_{100-x-y}$, and $Fe_xCo_yNi_{100-x-y}$, respectively. Small amounts of Ir and Pt impurities enhance magnetic moment in $Fe_xCo_yIr_{100-x-y}$ and $Fe_xCo_yPt_{100-x-y}$ systems. On the other hand, increasing amounts of Ni monotonically decrease magnetic moment in the $Fe_xCo_yNi_{100-x-y}$ system. These results are consistent with the results of MOKE and SQUID experiments.

Discussion

These experimental and theoretical results confirmed that the autonomous materials search system had discovered materials that had previously never been considered. Moreover, the discovery of novel materials can stimulate further theoretical studies. In this case, the materials found by the autonomous system led to a theoretical investigation of why these impurities (Ir and Pt) enhance the magnetization.

Figure 5a, b show the ab-initio simulation results of local magnetic moments of Fe and Co in the ternary alloy $Fe_{75}Co_{25}X_1$, where impurity X is a transition metal. Several elements around Ir

Fig. 3 Experimental confirmation by combinatorial XRD, MOKE, and SQUID experiments. a Illustration of combinatorial sputtering system with an automated moving mask for synthesizing $Fe_xCo_yIr_{100-x-y}$, $Fe_xCo_yPt_{100-x-y}$, and $Fe_xCo_yNi_{100-x-y}$ composition-spread thin films on SiO_2/Si substrates. **b** Composition map of $Fe_xCo_yIr_{100-x-y}$ composition-spread thin film, where the Ir composition gradient is along the X direction, and Fe and Co composition gradients are along opposite Y directions. The black spots denote sampling points of the combi-MOKE experiments. **c** Results of combi-XRD experiments with $Fe_xCo_yIr_{100-x-y}$ composition-spread sample. **d** XRD curve of $Fe_{68.1}Co_{26.2}Ir_{5.7}$ (bottom right point in Fig. 3b) **e** Results of combi-MOKE experiments with $Fe_xCo_yIr_{100-x-y}$ composition-spread sample. **f** MOKE curves of $Fe_{68.1}Co_{26.2}Ir_{5.7}$ (bottom right point in Fig. 3b). **g-i** Composition maps of $Fe_xCo_yIr_{100-x-y}$, $Fe_xCo_yPt_{100-x-y}$, and $Fe_xCo_yNi_{100-x-y}$ composition-spread thin films, respectively. **j-l** Mapping of amplitude of MOKE curves M_{MOKE} ($\propto$ saturation magnetization M_s) of the $Fe_xCo_yIr_{100-x-y}$, $Fe_xCo_yPt_{100-x-y}$, and $Fe_xCo_yNi_{100-x-y}$ composition-spread thin films, respectively. Small amounts of Ir and Pt impurities enhance the M_{MOKE}, while Ni impurity monotonically decreases the M_{MOKE}. **m** M_{MOKE} plots of $(Fe_{75.2}Co_{24.8})_{1-x}Ir_x$, $(Fe_{75.3}Co_{24.7})_{1-x}Pt_x$, and $(Fe_{71.1}Co_{28.9})_{1-x}Ni_x$ along dotted arrows in Fig. 3h–j, respectively. The dark-blue solid line and blue dotted line show theoretical M_{MOKE} values of pure Fe and $Fe_{75}Co_{25}$, respectively. **n, o** Magnetization curves obtained in SQUID experiments with $Fe_{73.2}Co_{24.2}Ir_{2.6}$, $Fe_{84.0}Co_{12.0}Pt_{4.0}$, $Fe_{75.2}Co_{24.8}$, and pure Fe at room temperature ($T = 300$ K) and low temperature ($T = 5$ K). The magnetization enhancement due to Ir and Pt impurities were also observed in the SQUID experiments.
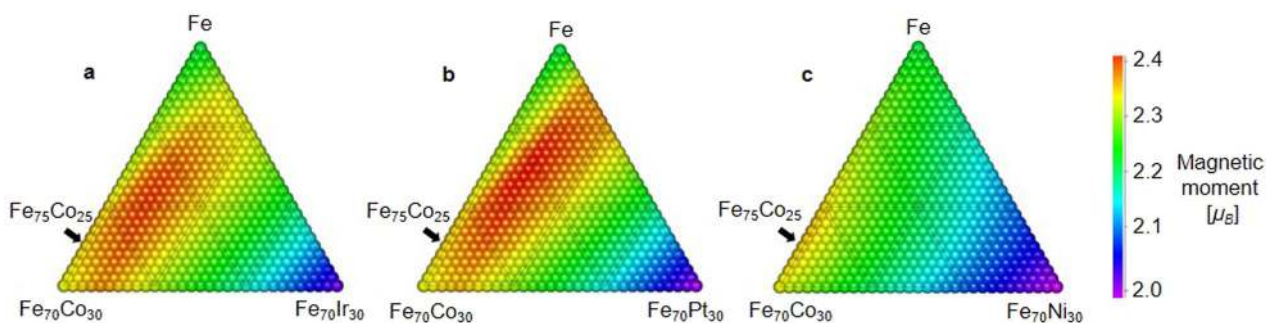

Fig. 4 Theoretical confirmation by ab-initio simulation. To confirm and analyze the alloy discovered by the autonomous materials search system and combinatorial experiments, the magnetic moments in various ternary alloys were investigated by ab-initio calculation. **a** Magnetic moments in FeCoIr ternary alloy system (largest magnetic moment was observed for $Fe_{81}Co_{15}Ir_4$). **b** Magnetic moments in FeCoPt ternary alloy system (largest magnetic moment was observed for $Fe_{85}Co_{11}Pt_4$). **c** Magnetic moments in FeCoNi ternary alloy system (Ni impurities do not enhance magnetic moment, so the largest magnetic moment was observed in the alloy at the top of the Slater–Pauling curve, $Fe_{75}Co_{25}$).

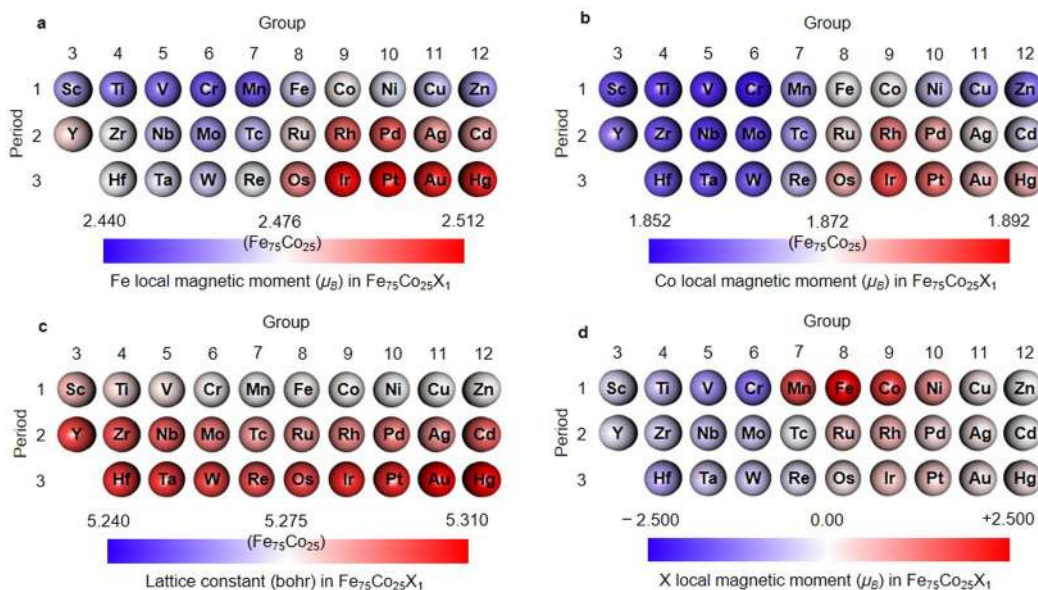**Fig. 5 Theoretical analysis by ab-initio simulation. a** Fe local magnetic moment in the $Fe_{75}Co_{25}X_1$ system, where X is a transition metal. The center of the color bar (white part) corresponds to the Fe local magnetic moment in $Fe_{75}Co_{25}$. Ir and Pt (and other elements around them in the periodic table) enhance the Fe local magnetic moment. **b** Co local magnetic moment in the $Fe_{75}Co_{25}X_1$ system. Ir and Pt (and other elements around them) also enhance the Co local magnetic moment. **c** Lattice constant of the $Fe_{75}Co_{25}X_1$ system. Elements with large atomic numbers tend to expand the lattice constant of $Fe_{75}Co_{25}$. **d** Local magnetic moments of different X elements in the $Fe_{75}Co_{25}X_1$ system. Positive and negative signs respectively mean parallel and anti-parallel magnetic moments with respect to the Fe and Co local magnetic moments. Paramagnetic elements, including Ir and Pt, have smaller magnetic moments than ferromagnetic elements (Fe, Co, and Ni).

and Pt in the periodic table increase the Fe and Co local magnetic moments. Figure 5c shows the lattice constant, which is thought to be one of the key parameters determining how the magnetic moment behaves in the $Fe_{75}Co_{25}X_1$ ternary alloys. Comparing Fig. 5a–c, one finds that not all elements that expand the lattice constant increase the Fe and Co local magnetic moments: Ta does not increase them even though $Fe_{75}Co_{25}Ta_1$ has a large lattice constant. Figure 5e shows the local magnetic moments of the X elements in $Fe_{75}Co_{25}X_1$ ternary alloys. Paramagnetic elements have much smaller local magnetic moments than ferromagnetic elements.

Our inductive theoretical study revealed that the $Fe_xCo_yIr_{100-x-y}$ and $Fe_xCo_yPt_{100-x-y}$ alloys have high magnetization because Ir and Pt impurities enhance the local magnetic moments of Fe and Co. However, too much Ir and Pt in the alloy reduces the magnetization because their local magnetic moments are small. Consequently, we observe the peaks of the $Fe_xCo_yIr_{100-x-y}$ and $Fe_xCo_yPt_{100-x-y}$ magnetization (magnetic moments) in the heat maps (Figs. 3j, k and 4a, b). This knowledge, that Ir and Pt impurities enhance local magnetic moment of Fe and Co, will contribute to the development of materials for even stronger magnets. Thus, the finding of an unexpected material by the autonomous materials search system will promote further experimental and/or theoretical studies.

In summary, stable alloys $Fe_xCo_yIr_{100-x-y}$ and $Fe_xCo_yPt_{100-x-y}$ with magnetization beyond that of Fe_3Co_1 were discovered via autonomous materials search system combining machine learning and ab-initio calculation. The performance of these alloys was confirmed by both experiments and theories. These alloys can be used for various applications, such as information storages, motors, sensors, actuators, and other electric devices. In addition, our inductive theoretical study based on the data-driven materials discovery revealed that the Ir and Pt impurities enhance the local magnetic moments of Fe and Co. This knowledge has a potential to contribute to the development of materials for even stronger magnets. Our autonomous system for materials discovery is quite versatile and can be used in the development of various materials by selecting appropriate objective properties and algorithms to be used in the virtual materials evaluation step and the next target composition/structure decision step. We believe that use of this autonomous system will lead to the emergence of more and more innovative materials and theories.

Methods

Game tree search. The game tree search algorithm[31] is used to calculate the priority P of a candidate next sampling point (composition). It tunes the trade-off between exploration and exploitation in the material search space, which in this case is an eight-dimensional space composed of the a, b, c, d, e, f, g, and h composition axes for the alloy $Fe_aCo_bNi_cRu_dRh_ePd_fIr_gPt_h$. The magnitude of the exploration is mathematically expressed as an expected uncertainty σ, which tends to be large at sparse points in the search space. The magnitude of exploitation is an expected value μ predicted on the basis of accumulated data. Both σ and μ are calculated using a Gaussian process regression model in which the objective variable and explanatory variables are respectively the total magnetic moment and the compositions (a, b, c, d, e, f, g, and h). To calculate the priority of a candidate next sampling point, we use an upper confidence bound (UCB) strategy[43] expressed as

$$P = \sigma + C\mu. \qquad (1)$$

Parameter C is used to tune the trade-off between exploration and exploitation. The cost of calculating P over the entire eight-dimensional materials search space is reduced by using a tree structure for the game tree search so that the spatial resolution increases stepwisely. The shallow part of the tree manages coarse-composition spatial resolution while the deep part manages fine-composition spatial resolution. Error pruning is used to exclude from the set of candidate next sampling points those with σ lower than threshold e_{min}. In this study, parameter C in the UCB formula (Eq. 1), initial spatial resolution d_0, tree depth D, and threshold e_{min} were set to 0.3, 0.8, 13, and 0.0001, respectively[31].

KKR-CPA. The Korringa–Kohn–Rostoker coherent potential approximation[32] is a Green's function-based density functional theory calculation often used for disordered

multicomponent alloys. Based on first-principles theory, it can predict various material properties, including the magnetic moment, from composition and crystal structure data. In this study we used Akai KKR software[32]. The crystal structural type ("brvtyp") was set to bcc. Lattice constant a between 5.27 and 5.38 bohr was optimized by minimizing the total energy. An imaginary part at the Fermi level ("edelt") and the width of the energy contour were set to 0.001 and 1.0 Ry, respectively. When calculating the magnetic moments in the FeCoX systems shown in Fig. 4, we set the relativistic treatment type ("reltyp") to "srals" including both the relativistic effect and spin-orbit interaction effect. In the KKR-CPA calculation for the autonomous materials search system shown in Fig. 2, the "reltyp" was set to "nrl", which means no relativistic effect or spin-orbit interaction effect, in order to reduce calculation cost. The "bzqlty" parameter, which specifies the quality of the Brillouin zone mesh, was set to 9. The maximum angular momentum taken into account ("xml") was 3. Note that the ab-initio calculation does not perfectly represent experimental results because of the condition difference. The experimental samples synthesized by sputtering were thin films, and their characterizations (MOKE, SQUID, XRD) were carried out at room temperature. The ab-initio calculations (KKR-CPA), on the other hand, were carried out assuming ideal disordered bulk states at absolute zero.

Limitation of the material search space. Ideally, the search for a material with a large magnetic moment would take place in a very large search space with axes for all metallic elements, but this is not feasible due to the computational cost and KKR-CPA performance limitation. There are more than 50 metallic elements in the periodic table, which is too large a number for KKR-CPA to converge in the Akai KKR software[32]. We therefore performed some calculation by hand beforehand. We calculated the local magnetic moments of various impurities in Fe, which is the likely main element in an alloy with a large magnetic moment. Supplementary Fig. S1 shows the KKR-CPA results for the local magnetic moment of various impurities (X) in $Fe_{99}X_1$ with a bcc structure. We identified eight elements (Fe, Co, Ni, Ru, Rh, Pd, Ir, and Pt) that have local magnetic moments greater than $+0.25\ \mu_B$. Because conventional materials simulation technologies (KKR-CPA in this case) are also being advanced, we should be able to simulate alloys with more components in the future. And in an expanded search space, the autonomous system might discover an alloy with even better properties.

Combinatorial experiment. To fabricate composition-spread thin film of $Fe_xCo_yIr_{100-x-y}$, $Fe_xCo_yPt_{100-x-y}$, and $Fe_xCo_yNi_{100-x-y}$ on a SiO_2/Si substrate, we employ a combinatorial sputtering system[36–39]. Using the moving mask motion, very thin unit layers with wedge shaped thickness are deposited and stacked alternatingly[38]. Because the thicknesses of the unit layers are about 0.2 nm, which is almost equal to the atomic distance, the ideal material mixtures can be obtained by using a post-deposition annealing process. We used a combinatorial sputtering system (CMS-6400)[38], whose ultimate vacuum is at 3×10^{-6} Pa. Sputtering using Fe, Ir, Pt, and Ni metal targets was done with a radio-frequency (RF) source, while that using a Co metal target was done with a direct current (DC) source. The alternative sputtering deposition was carried out aiming for 100 nm film thickness under an Ar atmosphere (40 sccm, 0.3 Pa) at room temperature. After deposition, films were annealed at 600 °C in vacuum (3×10^{-5} Pa) for 1 h. After the annealing process, film thickness was measured accurately by cross-sectional scanning electron microscopy (X-SEM). On the composition-spread sample, we carried out combinatorial longitudinal magneto-optic Kerr effect (combi-MOKE)[39] experiments at room temperature. To detect magneto-optical Kerr rotations (MOKE intensity), a magnetic field ranging from −650 to +650 Oe was applied in an in-plane direction. Sampling distances on the composition thin film were 2 mm and 3.3 mm for the x and y directions, respectively, as shown in Fig. 3b. After the combi-MOKE experiments, the composition-spread samples were cut into small tips (2 mm × 3.3 mm) by using the dicing machine for a superconducting quantum interference device (SQUID)[42] experiment. Lowering the temperature to 5 K was done by field cooling. To obtain magnetization curves, a magnetic field ranging from −400 to +400 Oe was applied in an in-plane direction.

Data availability
The data that support the results reported in this paper and other findings of this study are available from the corresponding author upon reasonable request.

Code availability
The code that supports the results reported in this paper and other findings of this study is available from the corresponding author upon reasonable request.

References
1. Spaldin, N. A. *Magnetic Materials: Fundamentals and Applications* (Cambridge Univ. Press, 2010).

2. Gutfleisch, O. et al. Magnetic materials and devices for the 21st century: stronger, lighter, and more energy efficient. *Adv. Mater.* **23**, 821–842 (2011).
3. Li, D., Li, Y., Pan, D., Zhang, Z. & Choi, C.-J. Prospect and status of iron-based rare-earth-free permanent magnetic materials. *J. Magn. Magn. Mater.* **469**, 535–544 (2019).
4. Cui, J. et al. Current progress and future challenges in rare-earth-free permanent magnets. *Acta Mater.* **158**, 118–137 (2018).
5. Snow, R. J., Bhatkar, H., N'Diaye, A. T., Arenholz, E. & Idzerda, Y. U. Large moments in bcc $Fe_xCo_yMn_z$ ternary alloy thin films. *Appl. Phys. Lett.* **112**, 7 (2018).
6. Kakehashi, Y. *Modern Theory of Magnetism in Metals and Alloys* (Springer-Verlag, 2012).
7. Butler, K. T., Davies, D. W., Cartwright, H., Isayev, O. & Walsh, A. Machine learning for molecular and materials science. *Nature* **559**, 547–555 (2018).
8. Mueller, T., Kusne, A. G. & Ramprasad, R. Machine learning in material science: recent progress and emerging applications. *Rev. Comput. Chem.* **29**, 186–273 (2016).
9. Jose, R. & Ramakrishna, S. Materials 4.0: materials big data enabled materials discovery. *Appl. Mater. Today* **10**, 127–132 (2018).
10. Senderowitz, H. & Tropsha, A. Materials informatics. *J. Chem. Inf. Model.* **58**, 2377–2379 (2018).
11. Ramprasad, R., Batra, R., Pilania, G., Mannodi-Kanakkithodi, A. & Kim, C. Machine learning in materials informatics: recent applications and prospects. *npj Comput. Mater.* **3**, 54 (2017).
12. Agrawal, A. & Choudhary, A. Perspective: materials informatics and big data: realization of the 'fourth paradigm' of science in materials science. *APL Mater.* **4**, 053208 (2016).
13. Lookman, T., Alexander, F. J. & Rajan, K. *Information Science for Materials Discovery and Design* (Springer, 2016).
14. Raccuglia, P. et al. Machine-learning-assisted materials discovery using failed experiments. *Nature* **553**, 73–77 (2016).
15. Lookman, T., Eidenbenz, S., Alexander, F. & Barnes, C. (eds) *Materials Discovery and Design by Means of Data Science and Optimal Learning* (Springer International Publishing, 2018).
16. Schmidt, J., Marques, M. R. G., Botti, S. & Marques, M. A. L. Recent advances and applications of machine learning in solid-state materials science. *npj Comput. Mater.* **5**, 83 (2019).
17. Burger, B. et al. A mobile robotic chemist. *Nature* **583**, 237–241 (2020).
18. Kusne, A. G. et al. On-the-fly machine-learning for high-throughput experiments: search for rare-earth-free permanent magnets. *Sci. Rep.* **4**, 6367 (2014).
19. Halder, A., Ghosh, A. & Dasgupta, T. S. Machine-learning-assisted prediction of magnetic double perovskites. *Phys. Rev. Mater.* **3**, 084418 (2019).
20. Sodeyama, K., Igarashi, Y., Nakayama, T., Tateyama, Y. & Okara, M. Liquid electrolyte informatics using an exhaustive search with linear regression. *Phys. Chem. Chem. Phys.* **20**, 22585–22591 (2018).
21. Wu, B., Han, S., Shin, K. G. & Lu, W. Application of artificial neural networks in design of lithium-ion batteries. *J. Power Sources* **395**, 128–136 (2018).
22. Stanev, V. et al. Machine learning modeling of superconducting critical temperature. *npj Comput. Mater.* **4**, 29 (2018).
23. Ishikawa, T., Miyake, T. & Shimizu, K. Materials informatics based on evolutionary algorithms: application to search for superconducting hydrogen compounds. *Phys. Rev. B* **100**, 174506 (2019).
24. Balachandran, P. V., Young, J., Lookman, T. & Rondinelli, J. M. Learning from data to design functional materials without inversion symmetry. *Nat. Commun.* **8**, 14282 (2017).
25. Balachandran, P. V., Kowalski, B., Sehirlioglu, A. & Lookman, T. Experimental search for high-temperature ferroelectric perovskites guided by two-step machine learning. *Nat. Commun.* **9**, 1668 (2018).
26. Iwasaki, Y. et al. Identification of advanced spin-driven thermoelectric materials via interpretable machine learning. *npj Comput. Mater.* **5**, 103 (2019).
27. Iwasaki, Y. et al. Machine-learning guided discovery of a new thermoelectric material. *Sci. Rep.* **9**, 2751 (2019).
28. Ishida, N., Wakamiya, A. & Saeki, A. Quantifying hole transfer yield from perovskite to polymer layer: statistical correlation of solar cell outputs with kinetic and energetic properties. *ACS Photonics* **3**, 1678–1688 (2016).
29. Takahashi, K., Takahashi, L., Miyazato, I. & Tanaka, Y. Searching for hidden perovskite materials for photovoltaic systems by combining data science and first principle calculations. *ACS Photonics* **5**, 771–775 (2018).
30. Sumita, M., Yang, X., Ishihara, S., Tamura, R. & Tsuda, K. Hunting for organic molecules with artificial intelligence: molecules optimized for desired excitation energies. *ACS Cent. Sci.* **4**, 1126–1133 (2018).
31. Sawada, R., Iwasaki, Y. & Ishida, M. Boosting material modeling using game tree search. *Phys. Rev. Mater.* **2**, 103802 (2018).
32. Akai, H. Electronic structure Ni-Pd alloys calculated by the self-consistent KKR-CPA method. *J. Phys. Soc. Jpn.* **51**, 468–474 (1982).
33. Khan, N. S., Staunton, J. B. & Stocks, G. M. Statistical physics of multicomponent alloys using KKR-CPA. *Phys. Rev. B* **93**, 054206 (2016).
34. Yang, L. et al. Investigation of the site preference in Mn_2RuSn using KKR-CPA-LDA calculation. *J. Magn. Magn. Mater.* **382**, 247–251 (2015).
35. Jin, K. et al. Tailoring the physical properties of Ni-based single-phase equiatomic alloys by modifying the chemical complexity. *Sci. Rep.* **6**, 20159 (2016).
36. Koinuma, H. & Takeuchi, I. Combinatorial solid-state chemistry of inorganic materials. *Nat. Mater.* **3**, 429 (2004).
37. Takeuchi, I. et al. Identification of novel compositions of ferromagnetic shape-memory alloys using composition spreads. *Nat. Mater.* **2**, 180–184 (2003).
38. Combinatorial Technology (Comet Inc. https://www.comet-nht.com/concept-e.html.)
39. Yoo, Y. K. et al. Identification of amorphous phases in the Fe-Ni-Co ternary alloy system using continuous phase diagram material chips. *Intermetallics* **14**, 241–247 (2006).
40. He, S. H., Zha, B. M. A., Zhang, Z. Z. & Jin, Q. Y. Formation of (002) texture in Fe films prepared by thermal treatment. *J. Magn. Mag. Mater.* **310**, 2656–2658 (2007).
41. Higo, T. et al. Large magneto-optical Kerr effect and imaging of magnetic octupole domains in an antiferromagnetic metal. *Nat. Photon.* **12**, 73–78 (2018).
42. Clarke, J. & Braginski, A. I. *The SQUID Handbook: Applications of SQUIDs and SQUID Systems* (John Wiley & Sons, 2006).
43. Auer, P. Using confidence bounds for exploitation-exploration trade-offs. *J. Mach. Learn. Res.* **3**, 397–422 (2002).

Acknowledgements

Author contributions

Y.I., R.S., and M.I. contributed to the theoretical discussion and the machine learning algorithm discussion. Y.I. wrote the manuscript. E.S. and M.I. supervised the study. All the authors discussed the results and commented on the manuscript.

Competing interests

The authors declare no competing interests.

Additional information

Supplementary information The online version contains supplementary material available at https://doi.org/10.1038/s43246-021-00135-0.

Correspondence and requests for materials should be addressed to Y.I.

Peer review information Primary handling editor: Aldo Isidori

Reprints and permission information is available at http://www.nature.com/reprints

Publisher's note Springer Nature remains neutral with regard to jurisdictional claims in published maps and institutional affiliations.